

Generating gradient germanium nanostructures by shock-induced amorphization and crystallization

Shiteng Zhao^a, Bimal Kad^b, Christopher E. Wehrenberg^c, Bruce A. Remington^c, Eric N. Hahn^a, Karren L. More^d, and Marc A. Meyers^{a,e,f,1}

^aMaterials Science and Engineering Program, University of California, San Diego, La Jolla, CA 92093; ^bDepartment of Structural Engineering, University of California, San Diego, La Jolla, CA 92093; ^cLawrence Livermore National Laboratory, Livermore, CA 94550; ^dOak Ridge National Laboratory, Oak Ridge, TN 37830; ^eDepartment of Mechanical and Aerospace Engineering, University of California, San Diego, La Jolla, CA 92093; and ^fDepartment of Nanoengineering, University of California, San Diego, La Jolla, CA 92093

Edited by Russell J. Hemley, The George Washington University, Washington, DC, and approved August 1, 2017 (received for review June 1, 2017)

Gradient nanostructures are attracting considerable interest due to their potential to obtain superior structural and functional properties of materials. Applying powerful laser-driven shocks (stresses of up to one-third million atmospheres, or 33 gigapascals) to germanium, we report here a complex gradient nanostructure consisting of, near the surface, nanocrystals with high density of nanotwins. Beyond there, the structure exhibits arrays of amorphous bands which are preceded by planar defects such as stacking faults generated by partial dislocations. At a lower shock stress, the surface region of the recovered target is completely amorphous. We propose that germanium undergoes amorphization above a threshold stress and that the deformation-generated heat leads to nanocrystallization. These experiments are corroborated by molecular dynamics simulations which show that supersonic partial dislocation bursts play a role in triggering the crystalline-to-amorphous transition.

amorphization | laser shock | nanocrystallization | germanium | gradient materials

Amorphous and gradient nanostructures are drawing intense attention due to their superior functional and mechanical properties (1, 2). Since they are thermodynamically metastable, amorphous materials can transform into nanocrystalline ones if appropriate treatments are applied (3). One of the most common methods to achieve amorphization is to quench a liquid at ultrafast cooling rates, which is extremely difficult for most pure elements (4). Alternatively, it has been shown that application of pressure leads to amorphization of materials whose melting point displays a negative Clapeyron slope ($dT/dP < 0$) (5–9); germanium (Ge) falls into this category (10). However, instead of pressure-induced amorphization, numerous studies, under both static (11, 12) and dynamic conditions (13–15), have shown that Ge undergoes a polymorphic transition at elevated pressures. Consequently, amorphization was not unambiguously identified in Ge until Clarke et al. (16) observed the indentation-induced crystalline-to-amorphous transition. More recently, a high-speed nanodroplet test also showed surface amorphization of Ge in an extremely localized manner (17).

Despite being widely studied, the underlying microstructural mechanisms of pressure-induced amorphization remain vague. This is due to the notorious brittleness of germanium at room temperature which renders its recovery from pressurization extremely challenging. The deposition of high-power pulsed-laser energy onto a millimeter-scale target generates transient states of extreme stresses that promptly build up and decay rapidly as the pulse propagates. The short duration of the stress pulse and impedance-matched encapsulation preserves the integrity of the target by suppressing the full development of cracks and enables postshock microstructure characterization. Using this methodology, we have previously reported shock-induced amorphization in silicon (18) and boron carbide (19). Before that, Jeanloz et al. (20) discovered this phenomenon in olivine (iron/magnesium silicate) subjected to shock compression. Amorphous bands formed on compression of crystalline silica were also observed in diamond anvil cell experiments (21, 22), where the role of stress in promoting the transition

was also pointed out. The important, albeit often ignored, role of shear in pressure-induced phase transition (21–24) is clearly evidenced by the directional nature of the amorphous bands.

Results

We performed the experiments at the Omega Laser Facility, Laboratory of Laser Energetics, University of Rochester, using a pulsed laser with a nominal square pulse shape (wavelength = 352 nm; laser duration = 1 ns). The nominal laser energies were $E_{\text{laser}} = 20 \sim 100$ J, resulting in intensities of $0.2 \sim 1.1$ TW/cm². Fig. 1A shows schematically the shock-recovery assembly. The high-density laser energy vaporizes the polystyrene (CH) ablator, which drives a compressive wave that eventually propagates into the [001] monocrystalline Ge target. For the 100-J experiment, the peak shock stress, $\sigma_{33} \approx 33$ GPa, can be inferred indirectly from the particle velocity (U_p) measurement by velocity interferometer system for any reflector (VISAR) (Fig. 1B–D) and impedance matching (Fig. 1E), as detailed in *Materials and Methods*. Note that the shock wave decays rapidly when traveling across the sample thickness, as evidenced by the significant drop of particle velocity at the rear surface (Ge/LiF interface) of the target (Fig. 1D). The time dependence of shock-wave propagation and decay of the longitudinal shock stress as function of depth can be simulated by 1D hydrodynamic simulation, as shown in Fig. S1.

Transmission electron microscopy (TEM) was used to inspect the postshock deformation micro- and nanostructure. The TEM samples were extracted by focused ion beam cutting from the as-shocked surface; the microstructural hierarchy is displayed in Fig. 2A. Along the direction of shock-wave propagation (left to right), nanocrystalline material can be observed as deep as 3 μm below the shock surface. Statistical analysis (Fig. 2B)

Significance

Amorphization and nanocrystallization are two powerful methods to tailor material properties by altering their microstructure without changing the overall chemistry. Using powerful laser-driven shocks, we demonstrate that amorphization and nanocrystallization can be achieved within a time scale that is considerably shorter than other conventional techniques. Our results provide compelling insights into pressure/shear amorphization and propose a route to fabricate gradient semiconducting nanostructures using lasers. Additionally, shear-driven amorphization is demonstrated as the dominant deformation mechanism in this extreme regime.

Author contributions: S.Z., B.A.R., and M.A.M. designed research; S.Z., B.K., C.E.W., and K.L.M. performed research; E.N.H. contributed new reagents/analytic tools; S.Z. and C.E.W. analyzed data; and S.Z. and M.A.M. wrote the paper.

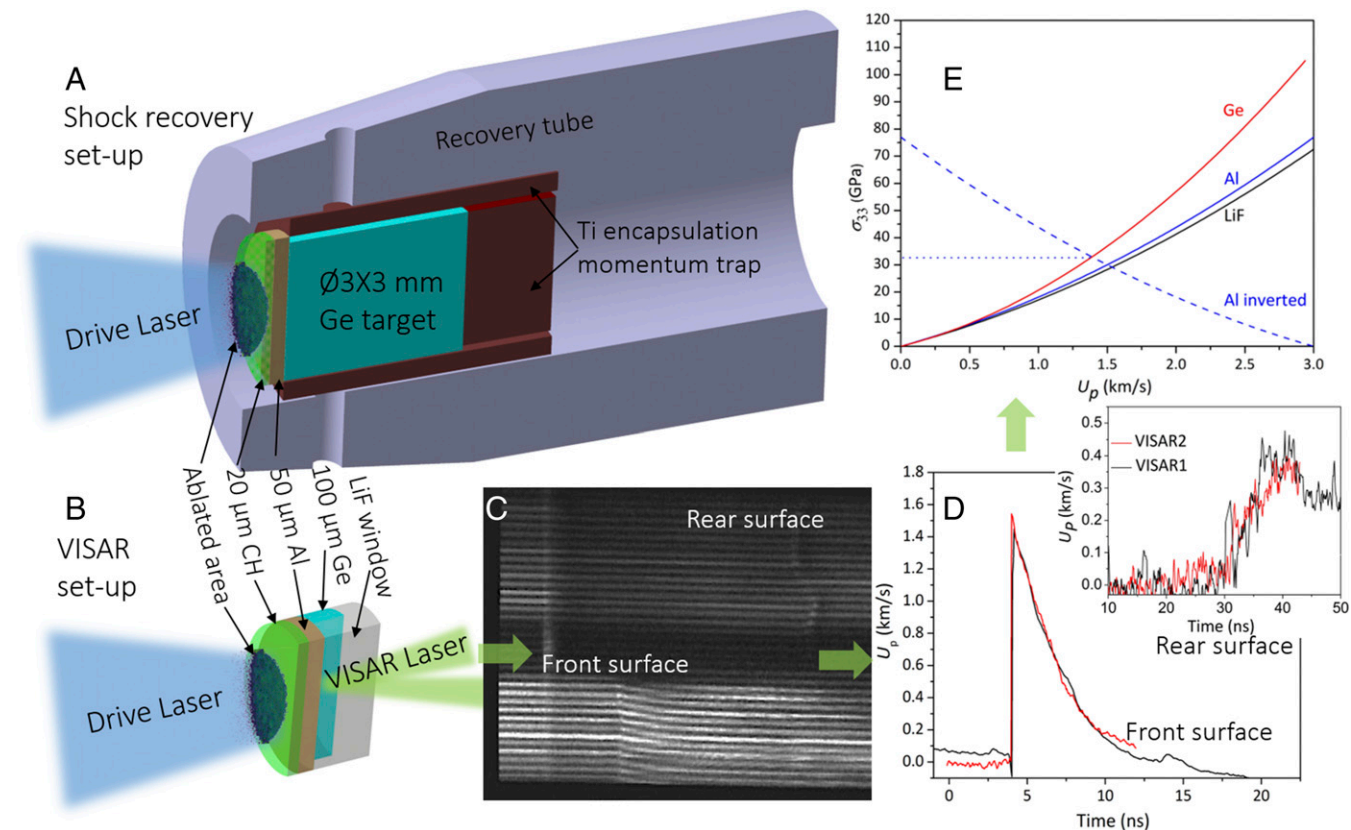
The authors declare no conflict of interest.

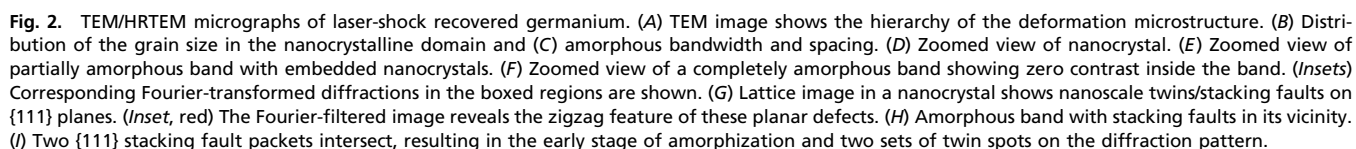
This article is a PNAS Direct Submission.

Freely available online through the PNAS open access option.

¹To whom correspondence should be addressed. Email: mameyers@eng.ucsd.edu.

This article contains supporting information online at www.pnas.org/lookup/suppl/doi:10.1073/pnas.1708853114/-DCSupplemental.





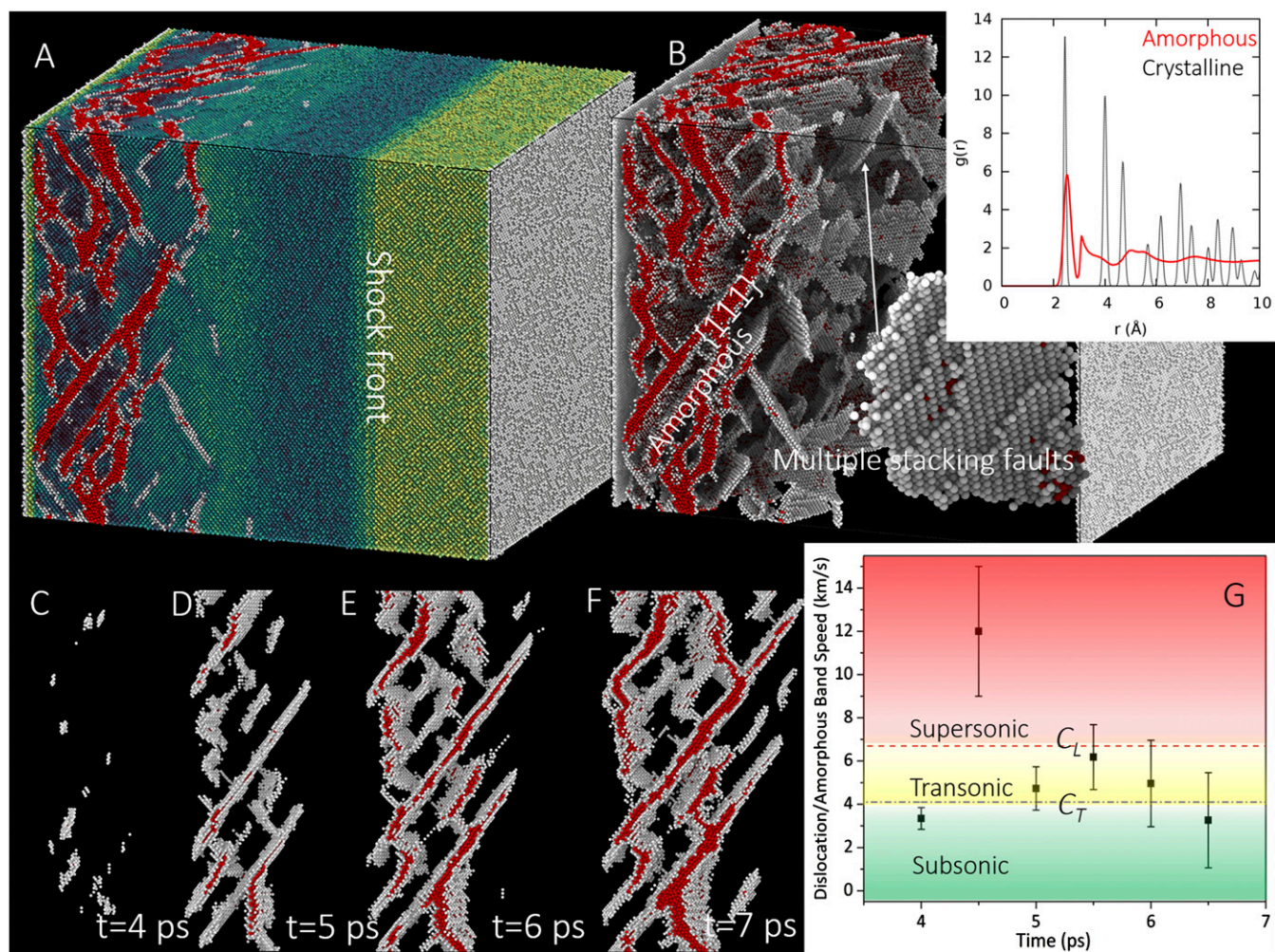


Fig. 3. MD simulation of partial dislocation propagation and amorphization: (A) Three-dimensional visualization of shocked germanium colored by coordination number. The amorphous bands are colored red. (B) Only the plastically deformed (defected) atoms are shown, suggesting that the amorphous bands are preceded by partial dislocations (stacking faults). The amorphous band aligns roughly with {111} slip plane. (Inset) Radial pair distribution functions distinguish the amorphous domain from crystalline structure. (C–F) Four snapshots showing the evolution of stacking faults and then amorphous bands. (G) Measurement of dislocation/amorphous band speed during shock compression and supersonic burst of dislocation is notified before the formation of amorphous band.

Discussion

Germanium melts with a reduction in volume and its melting temperature decreases as pressure increases [$dT/dP \approx -35$ K/GPa (30)]. Thus, compressive stresses favor amorphization because the disordered phase possesses a smaller specific volume than the original crystalline phase, although the amorphous state is energetically less favorable at ambient pressure. In addition to pressure, the superposed shear stress also facilitates amorphization by inducing large lattice displacements through stacking-fault generation and propagation (18). This is due to the nature of shock waves which generate a uniaxial strain with high-amplitude hydrostatic pressure (P) and shear stresses. The pressure (P) and the maximum shear stress (τ_{max}) are related through the generalized Hooke's law, as detailed in *SI Text* and Fig. S5. Specifically, the pressure dependency of elastic moduli and the ratio of shear stress over hydrostatic pressure is given in Fig. S5.

Applying classical nucleation theory we can obtain the pressure and shear-stress dependence of the nucleation barrier, as explained previously by Zhao et al. (31),

$$\Delta G_{c-a} = \Delta g_{c-a} \cdot \frac{4}{3} \pi r^3 - (P\varepsilon_v + \tau_{max}\gamma) \cdot \frac{4}{3} \pi r^3 + \gamma_{c/a} \cdot 4\pi r^2, \quad [1]$$

where ΔG_{c-a} is the energy gain of nucleating a spherical amorphous nucleus, $\Delta g_{c-a} = 14.2$ kJ/mol (32), and $\gamma_{c/a} = 0.08$ J/m² (32)

are the volumetric Gibbs free-energy barrier and crystalline/amorphous interfacial energy, respectively. ε_v and $\gamma \approx \varepsilon_v(1 + w_{spacing}/w_{band})$ are the volumetric and localized shear strain, which can be obtained from the Ge shock-Hugoniot data (ref. 33, pp. 521–568). The second term on the right-hand side of Eq. 1 represents the work done by pressure and shear, which help to overcome the energy barrier and interfacial energy gain of nucleating an amorphous embryo (expressed by the third term). Such an effect is plotted in Fig. 4A. The monotonically increasing energy as a function of radius curve for zero-stress state (blue) indicates the difficulty of forming amorphous phase at ambient state, whereas under shock the curves (red and yellow) are convex and exhibit a critical condition $dG_{c-a}/dr = 0$, corresponding to the critical nucleus size of $r_c = 2\gamma_{c-a}/(P\varepsilon_v + \tau_{max}\gamma - \Delta g_{c-a})$.

Shock-generated heat is another important factor in amorphization and subsequent nanocrystallization. Several effects have to be considered: (i) the temperature rise at the shock front reduces the energy barrier of crystalline-to-amorphous transition; (ii) upon further heat transfer, the newly formed amorphous structure can retransform into energetically more favorable crystalline phase; (iii) if the temperature is sufficiently high, shock-induced melting may occur; and (iv) the transient nature of the shock-induced thermal flux results in a self-quenching mechanism which leads to a hierarchical nanostructure.

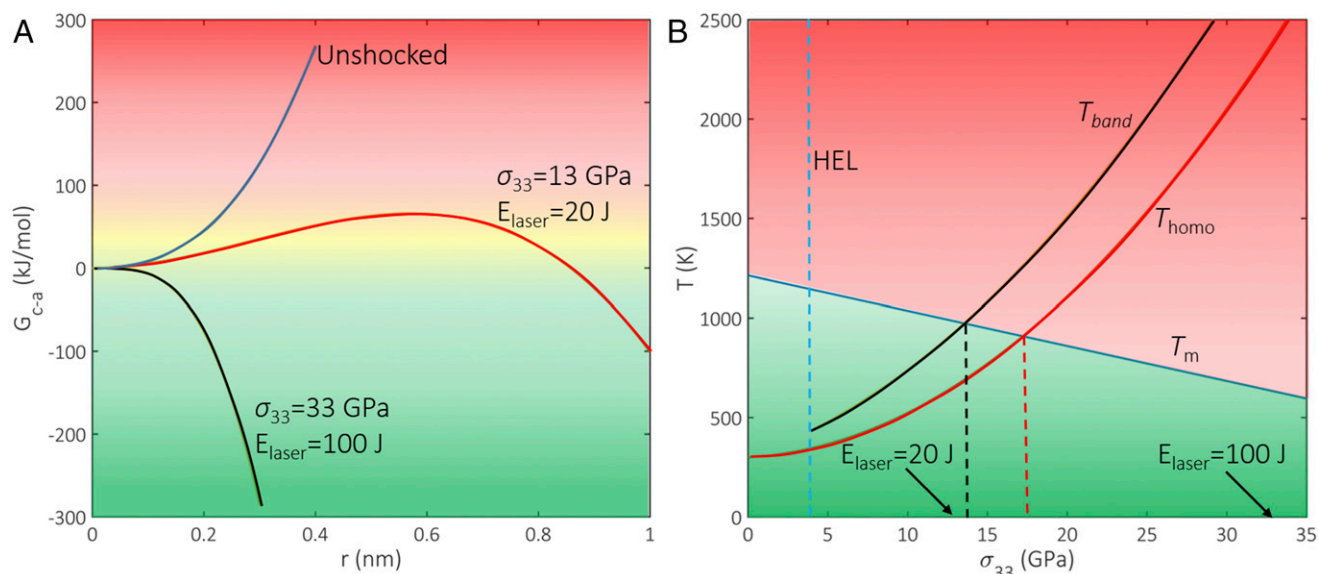


Fig. 4. Thermodynamic analysis of amorphization. (A) Gibbs free-energy change associated with nucleation of an amorphous embryo. The presence of shock stress (pressure plus shear) renders it possible to overcome the energy barrier of crystalline-to-amorphous transformation. (B) Pressure-induced homogeneous temperature (T_{homo}) and shear-induced localized temperature (T_{local}) compared with the decreasing melting temperature (T_m) as a function of shock stress (negative Clapeyron slope). The intersections represent the critical shock stresses of crystalline-to-amorphous transition, indicating that shear stress lowers the threshold.

The increase in temperature due to shock compression can be evaluated by considering both the homogeneous temperature rise (ΔT_{homo}) resulting from work done by hydrostatic pressure and the localized temperature rise (ΔT_{local}) resulting from work done by shear stress. The latter assumes a balance between relaxation of deviatoric strain energy and decrease in internal energy with heat loss to its surroundings, and thus gives a rough estimate of the temperature inside the amorphous band (19):

$$T_{band} = T_0 + \Delta T_{homo} + \Delta T_{local} \\ = T_0 + \frac{P\Delta V}{C_p} + \frac{2\dot{Q}w_{band}}{\sqrt{\pi}} \cdot \sqrt{\frac{t}{k\rho C_p}} \quad [2]$$

where T_0 is the preshock temperature, ΔV is the volume change, $\dot{Q} \approx \beta \tau_{max} \gamma / \Delta t$ is the rate of heat generation obtained from the conversion of deviatoric strain energy, β is the conversion efficiency (usually taken as 0.9), $\Delta t \sim 1$ ns is the duration of the laser pulse. k , ρ , C_p are the heat conductivity, density, and heat capacity of the amorphous band, respectively. It should be noted that the shear stress is assumed to be independent of shock stress after the Hugoniot elastic limit [~ 4 GPa for Ge (15)] as it is relaxed by plastic deformation. Fig. 4B shows the plot of shock-induced temperature together with melting temperature as a function of shock stress. The intersections of T_{homo} and T_{band} with T_m give the critical shock stresses (17.5 GPa for T_{homo} and 14 GPa for T_{band}) for the onset of amorphization. Clearly, the presence of shear stress lowers the threshold for amorphization, in agreement with early static compression experiments (21, 22). These calculations, whose accuracy depends largely on the material parameters, agree qualitatively with our experimental observations.

In summary, we have shown that germanium undergoes amorphization and nanocrystallization under extreme shock deformation. Although it is difficult, at this stage, to conclude whether these processes are solid state or the result of melting and quenching, the presence of shear stress is definitely crucial, and enhances the understanding of pressure-induced amorphization and polymorphisms (21, 22, 34–36). After its discovery in olivine

(20), shock-induced directional amorphization has now been confirmed in Si (18) and B_4C (19). Therefore, shear-induced amorphization should be considered as an important deformation mechanism in this extreme regime. More practically, our results suggest high-power, pulsed laser as a tool to rapidly produce substrate-free, micrometer-scale, gradient nanostructured semiconductors.

Materials and Methods

Laser Shock-Recovery Experiments. We performed laser-driven shock-recovery experiments at the Omega Laser Facility. The shock wave is created by the following sequence of processes. First, the high-power pulsed-laser energy is deposited on the 20- μ m CH ablator of the target package, ionizing it into plasma. Second, as the plasma flows away, the target surface experiences a reaction force equal to the rate at which momentum is carried away due to the rocket effect. The stress pulse promptly builds up and transforms into a shock wave. Third, the shock wave propagates inward and quickly decays as the laser duration is very short (1 ns). The amplitude of the ablation pressure (P_{abl}) can be estimated by the analytical model put forward by Lindl (37), $P_{abl} = C(1/\lambda)^\beta$, where C is a material-dependent constant and λ is the wavelength of the laser. $I = E_{laser}/At$ is the laser irradiance and β is the material-dependent exponential [calibrated to be 0.71 for diamond (38), which is similar to our CH ablator]. The target package consists of a 20- μ m CH ablator, 50- μ m Al foil, $\Phi 3 \times 3$ -mm cylindrical Ge target, and Ti momentum trap. The assembly is encapsulated within a Ti cup. The Al foil has two functions: (i) as a heat shield to minimize the preheating induced by laser irradiation; and (ii) as a pulse shaper to render the shock pulse on the target surface planar (uniaxial strain state). The laser pulse is nominally a 1-ns square pulse of 351 nm (3 omega) laser light. The beam was used without phase plates and defocused to a spot size of 3-mm diameter.

VISAR Analysis and Impedance Matching. Separate VISAR experiments were conducted to measure the particle velocity and further infer the shock pressure. A 532-nm probe laser is reflected from the rear surface of the moving target and then it will pass through collection optics and be routed into two separate streak cameras. Each of them uses a different etalon thickness. The VISAR target comprises a 20- μ m CH ablator, 50- μ m Al foil, a half-moon Ge sample (100- μ m thick), and laser-transparent LiF window. This specific geometry of the target allows the measurement of particle velocity of both front and rear surface of the Ge sample, which shows the rapid decay of the shock pressure as function of the depth. A correction factor of 0.775 is applied to the apparent velocity to account for the pressure dependence of the index of refraction of the LiF window. Conservation of mass and momentum give the relationship between the initial density ρ_0 , particle velocity U_p , shock velocity U_s and shock stress $\sigma_{33}, \sigma_{33} \approx \rho_0 U_s U_p$ (39), where $\rho_0 U_s$ is often termed

as shock impedance, which can be obtained from the slope of the shock Hugoniot curves (σ_{33} vs. U_p) in Fig. 1E. At the interface between the Al foil and Ge sample, shock wave is reflected and the shock stress changes. The inverted shock Hugoniot of Al (red dotted line in Fig. 1E) gives the estimate of the reflected shock wave and the intersection of this line with Ge curve (black line in Fig. 1E) yields the shock pressure on the front surface of the Ge sample. Such a process is termed as impedance matching. The shock stress at the rear surface of Ge sample can be read directly from the Ge Hugoniot curve.

Radiation-Hydrodynamic Simulations. Radiation-hydrodynamics simulations were performed using the HYADES code to aid in the design of the experiment and interpretation of the results. The target was modeled as a 1D stack consisting of 20- μm polystyrene ablator, 3 μm of glue (approximated as polystyrene), 50- μm Al, 3 μm glue (polystyrene), and 125 μm Ge. To simulate VISAR data, an additional layer of glue and LiF was substituted at the corresponding interface (front or back of the Ge). A rate-independent Steinberg–Guinan model was used to model the strength of Al (40). The Ge was modeled as elastic-perfectly plastic using the von Mises yield criterion with $Y_{\text{VM}} = 4$ GPa, consistent with observations of the Ge Hugoniot elastic limit.

TEM Sample Preparation and Observation. TEM is the ultimate tool to characterize the postmortem microstructure of the shocked target. To prepare TEM samples cite-specifically, a Hitachi NB5000 scanning electron microscope (SEM) equipped with a focused ion beam (FIB) was used to cut TEM samples directly from the laser-shocked germanium monocrystal surface. The TEM foils were ion milled by 30-kV Ga beam and finally polished at 5 kV to minimize FIB damage. The as-lifted sample is shown in the SEM image in Fig. S3B. A Hitachi HF3300 TEM operated at 300 keV was used to characterize the postshock microstructure. In addition to the results shown in the text (Fig. 2) where the Ge target was laser shocked with a high energy ($E_{\text{laser}} = 100$ J, $\sigma_{33} \sim 33$ GPa), Fig. S3C shows the microstructure of the Ge target shocked at a low energy ($E_{\text{laser}} = 20$ J, $\sigma_{33} \sim 10$ GPa). The contrast-less feature of the high-resolution TEM (HRTEM) image suggests the random arrangement of the atoms. The Fourier-transformed diffractograph exhibits a halo-shaped ring pattern, confirming the amorphous nature of the materials.

MD Simulations. MD simulations of shocked Ge were conducted using LAMMPS using the Tersoff potential under NVE (conservation of number of particles, volume, and total energy of the system) conditions. Shock compression was conducted along the [001] direction in single-crystalline germanium using a nonequilibrium drive piston. The piston was linearly accelerated to 1.2 km/s over 1 ps and held constant for the duration of the simulation. The system employs periodic boundaries perpendicular to the shock direction to create a uniaxial strain state. The lateral dimensions are 40 nm and the dimension along the direction of shock wave propagation is 50 nm to the rear surface. To compare the simulation to the experiments where the wave decays fully as it traverses the sample, analysis is only conducted before the reflection of the shock wave from the rear surface. The imparted particle velocity, $U_p = 1.2$ km/s, generates a shock pressure of 40.5 GPa and a concomitant deviatoric shear stress of 10.5 GPa. The corresponding shock speed is $U_s = 5.2$ km/s. Analysis of the shock-induced defect structure is completed using the “Identify Diamond Structure” implemented within OVITO (Open Visualization Tool) (41). To successfully apply this analysis technique to a strained lattice, an affine scale is first applied to artificially revert the strain such that analysis correctly identifies the defects. If this step is not completed the analysis tool identifies the uniaxially compressed region as unidentified non-dc atoms. Upon successful analysis, an affine scale exactly opposite in magnitude is applied to perfectly return the atoms to their original positions. Further analysis is conducted of the pair-distribution function (42) on the crystalline and amorphous regions. It describes the probability $g(r)$ of finding an atom at a given distance r away from any other atom. The shape and peaks of the curve can be used to differentiate between phases and can also provide coordination information.

ACKNOWLEDGMENTS. The enthusiastic help by Dorothy Coffey is deeply acknowledged. We acknowledge the highly professional support team of the Omega Laser Facility in the Laboratory of Laser Energetics, University of Rochester. Electron microscopy was conducted at the Center for Nanophase Materials Science (CNMS) User Facility, Oak Ridge National Laboratory, which is sponsored by the Office of Basic Energy Science, US Department of Energy. This research is funded by a University of California (UC) Research Laboratories Grant (09-LR-06-118456-MEYM), a National Nuclear Security Administration Grant (DE-NA0002930), and the UC Office of the President Laboratory Fees Research Program (LFR-17-449059). B.A.R. and C.E.W. also acknowledge the support of a US Department of Energy Grant (DE-AC52-07NA27344).

- Lu L, Shen Y, Chen X, Qian L, Lu K (2004) Ultrahigh strength and high electrical conductivity in copper. *Science* 304:422–426.
- Thevamaran R, et al. (2016) Dynamic creation and evolution of gradient nanostructure in single-crystal metallic microcubes. *Science* 354:312–316.
- Thompson M, Galvin G, Mayer J (1984) Melting temperature and explosive crystallization of amorphous silicon during pulsed laser irradiation. *Phys Rev Lett* 52:2360–2364.
- Zhong L, Wang J, Sheng H, Zhang Z, Mao SX (2014) Formation of monatomic metallic glasses through ultrafast liquid quenching. *Nature* 512:177–180.
- Sharma SM, Sikka SKK (1996) Pressure induced amorphization of materials. *Prog Mater Sci* 40:1–77.
- Machon D, Meersman F, Wilding MC, Wilson M, McMillan PF (2014) Pressure-induced amorphization and polymorphism: Inorganic and biochemical systems. *Prog Mater Sci* 61:216–282.
- Mishima O, Calvert LD, Whalley E (1984) “Melting ice” I at 77 K and 10 kbar: A new method of making amorphous solids. *Nature* 310:393–395.
- Deb SK, Wilding M, Somayazulu M, McMillan PF (2001) Pressure-induced amorphization and an amorphous-amorphous transition in densified porous silicon. *Nature* 414:528–530.
- Grocholski B, Speziale S, Jeanloz R (2010) Equation of state, phase stability, and amorphization of Si4 at high pressure and temperature. *Phys Rev B* 81:1–7.
- Nesterenko VF (1984) Scope for producing supercooled melts by a dynamic method. *Combust Explos Shock Waves* 19:665–667.
- Jamieson JC (1963) Crystal structures at high pressures of metallic modifications of silicon and germanium. *Science* 139:762–764.
- Oliver DJ, Bradby JE, Williams JS, Swain MV, Munroe P (2009) Rate-dependent phase transformations in nanoindeented germanium. *J Appl Phys* 105:40–43.
- Pavlovskii MN (1967) Formation of metallic modification of Germanium and Silicon under shock loading. *Sov Phys Solid State* 9:2514–2518.
- Graham RA, Jones OE, Holland JR (1966) Physical behavior of germanium under shock wave compression. *Solid State Commun* 27:1519–1529.
- Gust WH, Royce EB (1972) Axial yield strengths and phase-transition stresses for <100>, <110>, and <111> germanium. *J Appl Phys* 43:4437–4442.
- Clarke DR, Kroll CM, Kirchner PD, Cook RF, Hockey BJ (1988) Amorphization and conductivity of silicon and germanium induced by indentation. *Phys Rev Lett* 60:2156–2159.
- Gamero-Castaño M, Torrents A, Borrajo-Pelaez R, Zheng J-G (2014) Amorphization of hard crystalline materials by electrospun nanodroplet impact. *J Appl Phys* 116:174309.
- Zhao S, et al. (2015) Pressure and shear induced amorphization of silicon. *Extrem Mech Lett* 5:74–80.
- Zhao S, et al. (2016) Directional amorphization of boron carbide subjected to laser shock compression. *Proc Natl Acad Sci USA* 113:12088–12093.
- Jeanloz R, et al. (1977) Shock-produced olivine glass: First observation. *Science* 197:457–459.
- Kingma KJ, Meade C, Hemley RJ, Mao HK, Veblen DR (1993) Microstructural observations of a-quartz amorphization. *Science* 259:666–669.
- Hemley RJ, Jephcoat AP, Mao HK, Ming LC, Manghnani MH (1988) Pressure-induced amorphization of crystalline silica. *Nature* 334:52–54.
- Levitas VI, Ravelo R (2012) Virtual melting as a new mechanism of stress relaxation under high strain rate loading. *Proc Natl Acad Sci USA* 109:13204–13207.
- Levitas VI (2005) Crystal-amorphous and crystal-crystal phase transformations via virtual melting. *Phys Rev Lett* 95:075701.
- Bhat MH, et al. (2007) Vitrification of a monatomic metallic liquid. *Nature* 448:787–790.
- Solomon VC, et al. (2008) Electron microscopy study of germanium glass vitrified by high pressure melt – quench. *Microsc Microanal* 14:1138–1139.
- Tersoff J (1988) Empirical interatomic potential for silicon with improved elastic properties. *Phys Rev B Condens Matter* 38:9902–9905.
- Plimpton S (1995) Fast parallel algorithms for short-range molecular dynamics. *J Comput Phys* 117:1–19.
- Gumbach P, Gao H (1999) Dislocations faster than the speed of sound. *Science* 283:965–968.
- Jayaraman A, Klement JRW, Kennedy GC (1963) Melting and polymorphism at high pressures in some group IV elements and III-V compounds with the diamond/zinc-blende structure. *Phys Rev* 130:540–547.
- Zhao S, et al. (2016) Amorphization and nanocrystallization of silicon under shock compression. *Acta Mater* 103:519–533.
- Sandoval L, Reina C, Marian J (2015) Formation of nanotwin networks during high-temperature crystallization of amorphous germanium. *Sci Rep* 5:17251.
- McQueen RG, Marsh SP (1970) The equation of state of solids from shock wave studies. *High Velocity Impact Phenomena*, ed Kinslow R (Academic, New York), pp 293–417.
- McMillan PF, Wilson M, Daisenberger D, Machon D (2005) A density-driven phase transition between semiconducting and metallic polymorphs of silicon. *Nat Mater* 4:680–684.
- Corsini NR, et al. (2015) Pressure-induced amorphisation and a new high density amorphous metallic phase in matrix-free Ge nanoparticles. *Nano Lett* 15:7334–7340.
- McMillan PF (2002) New materials from high-pressure experiments. *Nat Mater* 1:19–25.
- Lindl J (1995) Development of the indirect-drive approach to inertial confinement fusion and the target physics basis for ignition and gain. *Phys Plasmas* 2:3933–4024.
- Fratanduono DE, et al. (2011) Refractive index of lithium fluoride ramp compressed to 800 GPa. *J Appl Phys* 109:123521.
- Meyers MA (1994) *Dynamic Behavior of Materials* (John Wiley & Sons, New York), pp 189–191.
- Steinberg DJ, Cochran SG, Guinan MW (1980) A constitutive model for metals applicable at high-strain rate. *J Appl Phys* 51:1498–1504.
- Stukowski A (2010) Visualization and analysis of atomistic simulation data with OVITO—the Open Visualization Tool. *Model Simul Mater Sci Eng* 18:15012.
- Levine BG, Stone JE, Kohlmeier A (2011) Fast analysis of molecular dynamics trajectories with graphics processing units-radial distribution function histogramming. *J Comput Phys* 230:3556–3569.

Supporting Information

Zhao et al. 10.1073/pnas.1708853114

SI Text

Shear Stresses Under Shock Compression. The shock stress (σ_{33}), hydrostatic pressure (P), and maximum shear stress (τ_{max}) can be obtained from the generalized Hooke's law for uniaxial strain, $\sigma_{ij} = C_{ijkl}\epsilon_{33}$, where C_{ijkl} is the elastic constants, ϵ_{33} is the uniaxial strain, and x_3 is the direction of shock-wave propagation. The ratio τ_{max}/P can be expressed as a function of elastic stiffness (if the deformation is assumed to be purely elastic) as

$$\frac{\tau_{max}}{P} = \frac{3(C_{11} - C_{12})}{2(C_{11} + 2C_{12})}. \quad [S1]$$

For germanium, at ambient pressure, $C_{11} = 129.2$ GPa, $C_{12} = 47.9$ GPa, rendering $\tau_{max}/P \approx 0.54$. This is a first approximation since the elastic moduli are pressure-dependent as predicted by our MD simulations. This high shear stress is relaxed by directional deformation and subsequent amorphous band formation.

Supersonic Dislocation. Both our TEM observations and MD simulations show that dislocation (stacking faults) activity occurs before the amorphization, suggesting that dislocations are the trigger to the drastic crystalline-to-amorphous transition. Therefore, it is reasonable to infer that the kinetics of dislocation motion determine the kinetics of amorphization. It has been predicated by the theory of linear elasticity that the dislocation velocity is limited by the transverse wave speed (C_T) at which the energy associated with the screw dislocation approaches infinity, as shown in Eq. S2.

$$\frac{W}{l} = \frac{Gb^2}{4\pi\left(1 - \frac{v_d^2}{C_T^2}\right)^{1/2}} \ln \frac{R}{b}, \quad [S2]$$

where W is the elastic energy associated with a moving screw dislocation, l is the length, and b is the Burgers vector. However, MD simulations by Gumbsch and Gao (29) suggested the existence of supersonic dislocation in tungsten, even above longitudinal sound speed. Gumbsch and Gao (29) proposed that a supersonic dislocation can be obtained if an ultrafast dislocation seed is nucleated at a stress concentrator. An applied stress is required to help the dislocation to overcome the sound barrier. Such a condition can be most likely achieved in a strong shock experiment where the high stress state (both hydrodynamic and deviatoric components) builds up quickly at the shock front. In our MD simulations, supersonic dislocation bursts are identified, as shown in Fig. 3, before amorphization. The motion of dislocation is nonuniform at this stage and the velocity should be a range instead of a constant. After such a supersonic event, the dislocation velocity quickly falls off when the amorphization is initiated; the motion of dislocation/amorphous band becomes transonic and uniform. Movie S1 and MD snapshots in Fig. 3 show how the partial dislocations nucleate, catch up with the shock front, and eventually give rise to the formation of amorphous bands.

Estimation of Sound Speeds and Dislocation Velocity. Travel of acoustic waves in crystal is highly anisotropic and orientation dependent. Germanium is a cubic material and the active slip system is of $\{111\}\langle 110 \rangle$ type. Thus, we need to evaluate the sound speeds along the $\langle 110 \rangle$ direction to compare them with the dislocation velocity. The corresponding longitudinal sound speed is

$$C_L = \left(\frac{C_{11} + C_{12} + 2C_{44}}{2\rho} \right)^{1/2}. \quad [S3]$$

The transversal sound speed is polarized in different $\langle 110 \rangle$ directions:

$$C_{Tmax} = \left(\frac{C_{44}}{\rho} \right)^{1/2},$$

$$C_{Tmin} = \left(\frac{C_{11} - C_{12}}{2\rho} \right)^{1/2}. \quad [S4]$$

It should be noted that the elastic constants C_{11} , C_{12} , C_{44} are a function of pressure, as shown in Fig. S5A. Thus, the sound speeds also depend on pressure, as plotted in Fig. S4.

Dislocation velocity (V_d) is estimated by tracking the displacement of the defects in time. Multiple snapshots with 1-ps spacing (in MD time) are used and the effective defect length is measured from each snapshot. It should be noted that the motion/growth of these defects is not strictly limited in one particular direction and we also notice the lateral growth of the stacking faults/amorphous bands, suggesting the activation of stacking faults in the adjacent slip planes. Due to these complexities, the defect velocity was measured several times to minimize the errors caused by the uncertainty of the defect length. Despite the error bars, our measurements in Fig. 3G of the main text show that the partial dislocations nucleate with an ultrafast velocity ($V_d \sim C_T$) right after the shock front passes by. Shortly after their nucleation, the dislocations are still under extremely high stresses and they quickly accelerate to the supersonic ($V_d > C_L$) regime. However, the motion of supersonic dislocations is not steady state, i.e., the velocity should be a range instead of a number. After such an explosive motion/growth, their velocity falls to the transonic regime ($C_L > V_d > C_T$). The supersonic dislocations seem to trigger the amorphization which helps to relax the concentrated deviatoric stress.

Calculation of the Structure Factor. To better understand the structure of the amorphous germanium, we have thus calculated the $S(Q)$ profile based on our selected area electron diffraction pattern. The result is given in the following figure, Fig. S2. It should be mentioned that the diffractograph that we show in the article is the FFT of the HRTEM image where we can easily distinguish the pattern of amorphous materials from that of crystalline domain. However, the FFT diffractograph is not suitable for the calculation of the structure factor $S(Q)$. Therefore, additional experiments were conducted and the selected area electron diffraction pattern (in the vicinity of the band) is recorded in Fig. S2B. However, the size of the diffraction aperture is much larger than the characteristic size of the amorphous band (~ 20 nm) and hence the pattern is inevitably contaminated by the surrounding crystalline matrix, which affects the calculation of the $S(Q)$. Another factor is that the microscope does not have an energy filter and therefore cannot filter the inelastically scattered electrons. Thus, the tail becomes very noisy and therefore we trimmed it at $Q \sim 6 \text{ \AA}^{-1}$. Nevertheless, the first two broad peaks on the $S(Q)$ vs. Q curve correspond mostly to the amorphous structure and we found that they are very similar to the results shown by ref. 25, albeit with a little shift to the right (higher value of scattering vector, Q), indicating that the amorphous structure may be a low-density amorphous polymorph, which may form under unloading.

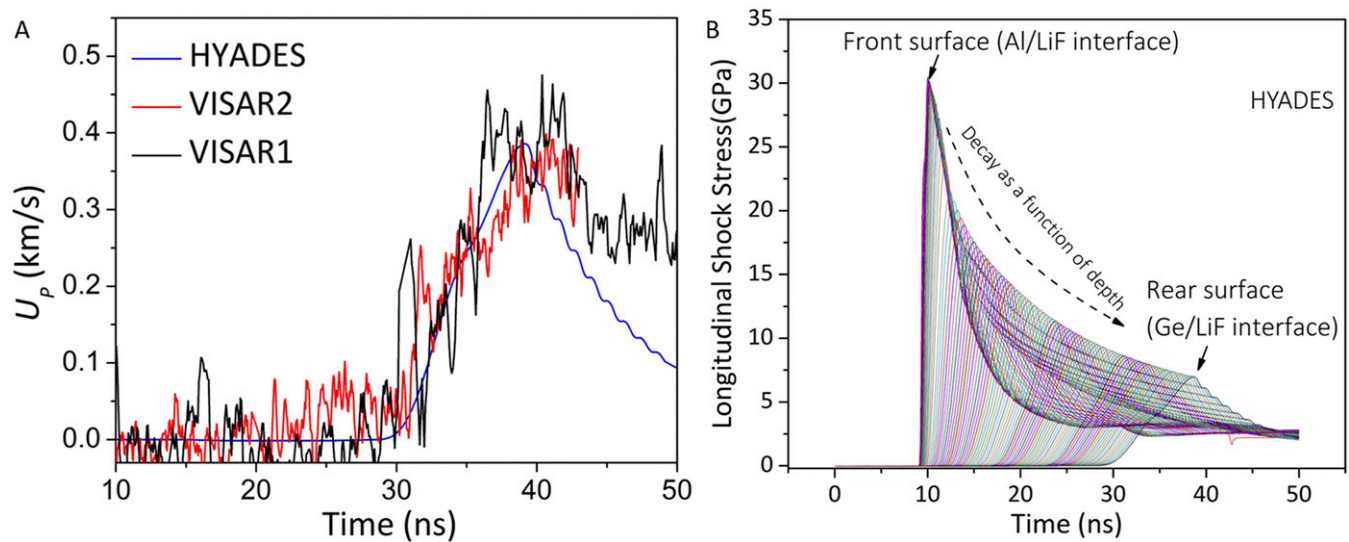


Fig. 51. HYADES simulation of shock-wave propagation and decay in Ge. (A) Calibration of the simulation with the experimentally determined velocity profile at the Ge/LiF interface (rear surface). (B) Simulated longitudinal shock stress vs. time profile at different depths below the shock surface, showing the decay of the amplitude of the stress wave as it passes through the material.

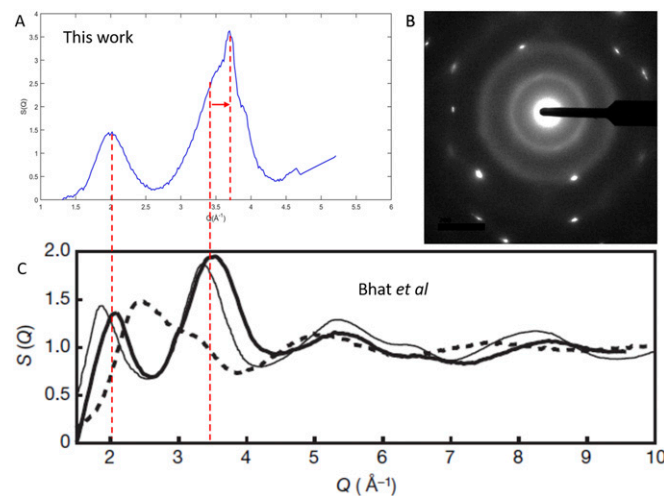


Fig. 52. (A) Calculated $S(Q)$ from the electron diffraction pattern in B and compared with previous reports by Bhat et al. (25) in C.

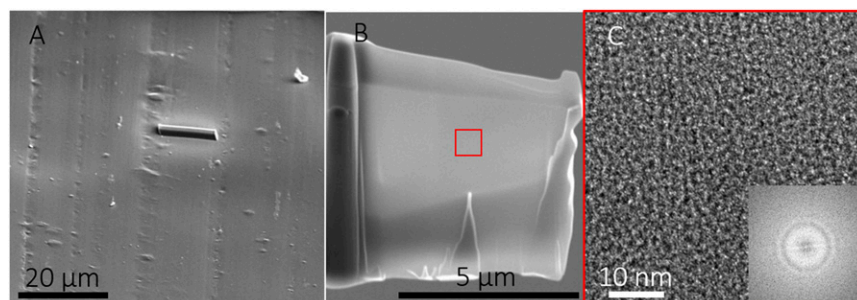


Fig. 53. Micrographs of Ge shocked at a lower laser energy (20 J). (A) SEM image of the shocked surface of [001] Ge single crystal. The rectangle indicates the position of the TEM sample cut by FIB technique. (B) SEM image of the TEM sample cross-section. (C) HRTEM image shows that the deformed structure is indeed amorphous without long-range order. The amorphous feature can be also confirmed by FFT diffractography in the bottom-left corner.

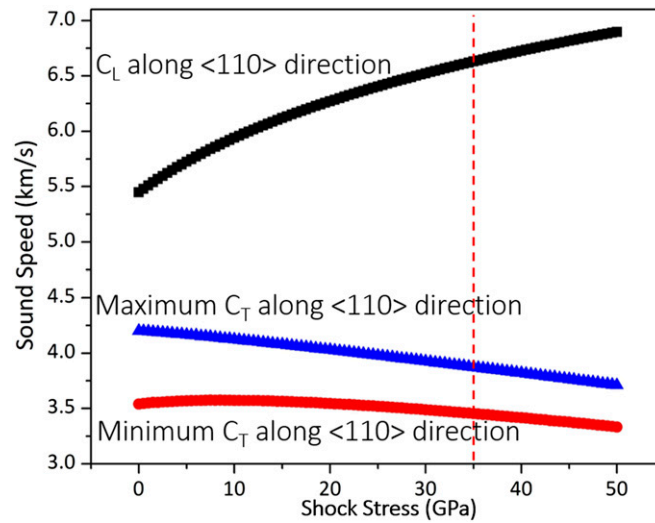


Fig. S4. Pressure dependency of longitudinal sound speed, transverse sound speed (split into two different values due to crystal anisotropy) along the $\langle 110 \rangle$ slip direction. The intersection of the vertical red dotted line with the black line gives the longitudinal sound speed at the pressure matched with the condition of the MD simulation (roughly agrees with experiment as well).

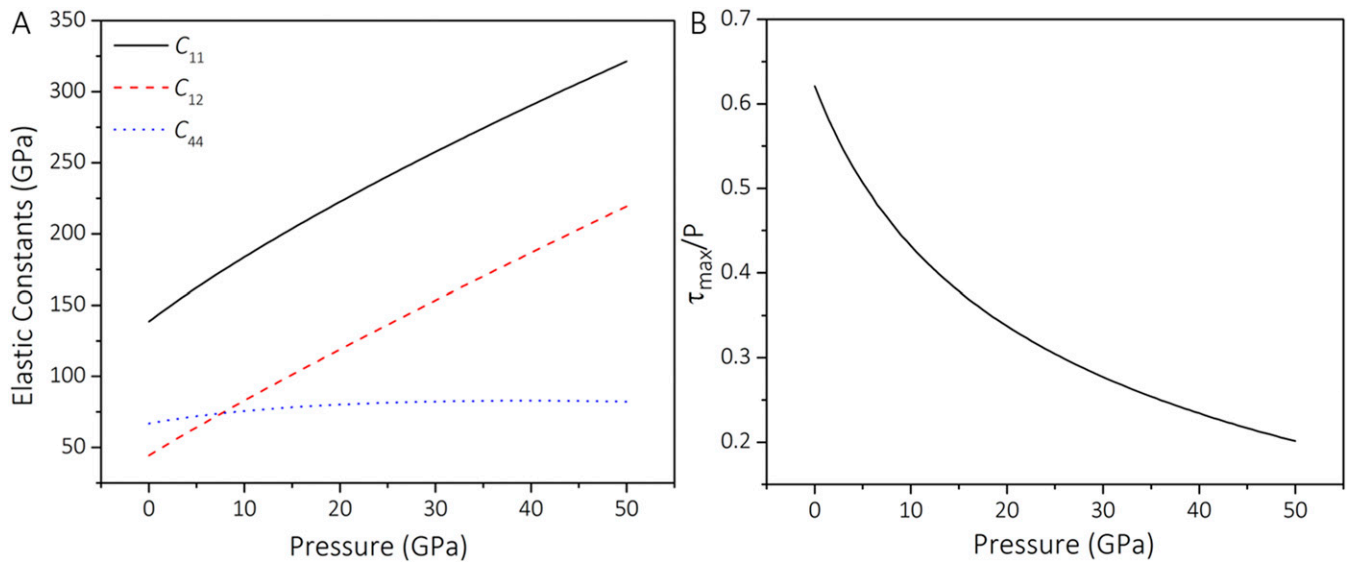
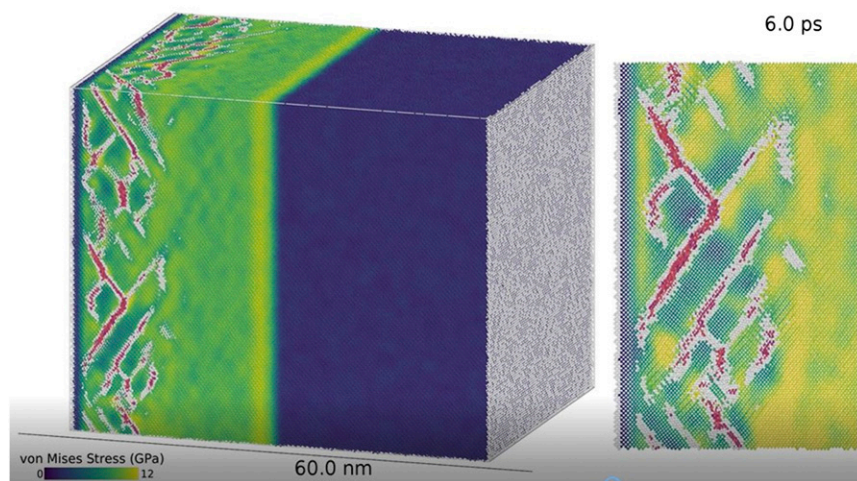


Fig. S5. (A) MD prediction of pressure dependency of elastic constant and (B) ratio of maximum shear over pressure (assuming elasticity and no relaxation).



Movie S1. Movie of MD simulation snapshots captures the process of shock-induced amorphization. (*Left*) Three-dimensional view of the entire simulation box. (*Right*) Two-dimensional projection on the (110) plane in the vicinity of the transformation regime. The movie is colored by von Mises stress (gigapascals). Directional amorphization occurs after the passage of the shock front.

[Movie S1](#)